

Published in final edited form as:

Nat Mater. 2022 October ; 21(10): 1150–1157. doi:10.1038/s41563-022-01321-2.

Dielectric control of reverse intersystem crossing in thermally activated delayed fluorescence emitters

Alexander J. Gillett^{#1,*}, Anton Pershin^{#2,3}, Raj Pandya¹, Sascha Feldmann¹, Alexander J. Sneyd¹, Antonios M. Alvertis¹, Emrys W. Evans^{1,4}, Tudor H. Thomas¹, Lin-Song Cui⁵, Bluebell H. Drummond¹, Gregory D. Scholes⁶, Yoann Olivier⁷, Akshay Rao¹, Richard H. Friend¹, David Beljonne^{2,*}

¹Cavendish Laboratory, University of Cambridge, JJ Thomson Avenue, Cambridge, CB3 0HE, UK

²Laboratory for Chemistry of Novel Materials, Université de Mons, Place du Parc 20, 7000 Mons, Belgium

³Wigner Research Centre for Physics, PO Box 49, H-1525, Budapest, Hungary

⁴Department of Chemistry, Swansea University, Singleton Park, Swansea, SA2 8PP, UK

⁵CAS Key Laboratory of Soft Matter Chemistry, Department of Polymer Science and Engineering, University of Science and Technology of China, Hefei, 230026, China

⁶Department of Chemistry, Princeton University, Princeton, New Jersey 08544, United States

⁷Unité de Chimie Physique Théorique et Structurale & Laboratoire de Physique du Solide, Namur Institute of Structured Matter, Université de Namur, Rue de Bruxelles, 61, 5000 Namur, Belgium

These authors contributed equally to this work.

Abstract

Thermally-activated delayed fluorescence (TADF) enables organic semiconductors with charge transfer (CT)-type excitons to convert dark triplet states into bright singlets via reverse intersystem crossing (rISC). However, thus far the contribution from the dielectric environment has received insufficient attention. Here, we study the role of the dielectric environment in a range of TADF materials with varying changes in dipole moment upon optical excitation. In dipolar emitters, we observe how environmental reorganisation after excitation triggers the full CT exciton formation, minimising the singlet-triplet energy gap, with the emergence of two (reactant-inactive) modes acting as a vibrational fingerprint of the CT product. In contrast, the dielectric environment plays a

Users may view, print, copy, and download text and data-mine the content in such documents, for the purposes of academic research, subject always to the full Conditions of use: <https://www.springernature.com/gp/open-research/policies/accepted-manuscript-terms>

*Corresponding authors: David Beljonne: david.beljonne@umons.ac.be; Alexander J. Gillett: ajg216@cam.ac.uk.

Author contributions

A.J.G. and A.P. contributed equally. A.J.G, R.H.F. and D.B. conceived the work. A.J.G. performed the TA measurements. A.J.G., R.P. and A.J.S. carried out the IVS measurements. S.F. performed the TGPL measurements. E.W.E., T.H.T. and B.H.D. carried out the trPL measurements. E.W.E. measured the PLQE. T.H.T. performed the Raman spectroscopy. A.J.G., E.W.E and L.-S.C. fabricated the samples used in the work. A.P. carried out the quantum chemical calculations. A.M.A., G.D.S, Y.O. and D.B. discussed the calculation results. A.R., R.H.F. and D.B. supervised their group members involved in the project. A.J.G., A.P., G.D.S., R.H.F. and D.B. wrote the manuscript with input from all authors.

Competing interests

The authors declare no competing interests.

smaller role in less dipolar materials. The analysis of energy-time trajectories and their free-energy functions reveal that the dielectric environment significantly reduces the activation energy for rISC in dipolar TADF emitters, increasing the rISC rate by three orders of magnitude versus the isolated molecule.

Organic light emitting diodes (OLEDs) based on materials that exhibit thermally activated delayed fluorescence (TADF) have gained significant attention for their ability to utilize dark triplet excitons for light emission *via* a thermally-assisted reverse intersystem crossing (rISC) process¹⁻⁴. As a result, the internal quantum efficiencies of TADF OLEDs can now approach 100%^{1-3,5-7}. However, despite the substantial effort to understand the mechanism of rISC in TADF emitters⁸⁻¹¹, relatively little attention has been given to the role of the surrounding dielectric environment in this process¹²⁻¹⁷.

Due to the charge transfer (CT) nature of their excited states, TADF materials often exhibit large changes in their dipole moment upon optical or electrical excitation, which can exceed 20 D^{13,18}. This change in dipole moment will induce a reorientation of the local dielectric environment to better stabilize the new electrostatic configuration of the chromophore^{19,20}. Such effects are not limited to solution environments where the solvent can freely rotate²¹⁻²³, but have also been observed in solid films comprising TADF emitters dispersed in both polymer and small molecule hosts^{13,24,25}. These environmental reorganization effects can have a significant impact on the electronic properties of the molecule, including large shifts in the optical band gap, modulation of the coupling between electronic states, and even changes in the relative energetic ordering of the CT and local triplet exciton (³LE) states^{13,24}. In this work, we reveal the interplay between the TADF emitter and the environment, highlighting the remarkable role of the dielectric environment in gating the rISC process of dipolar TADF materials.

Results

We have investigated five high-performance TADF materials that represent popular structural motifs (Fig. 1a), including linear donor-acceptor (D-A; TXO-TPA and DACT-II)^{26,27}, D-A-D (2CzPN)¹ and multi-D systems (4CzIPN and 5CzTRZ)^{1,21}. The structures of the three wide-gap materials chosen to represent solution (toluene), small molecule (UGH2), and polymer (polystyrene) host environments are shown in Fig. 1b. To restrict the variables as far as possible, all host materials have been chosen to possess both similar structural motifs and comparable dielectric constants of between 2.4-2.8 (Fig. S1)²⁸⁻³⁰. These dielectric constants are low compared to many other organic semiconductors used as OLED host materials³¹, meaning that our results represent a lower bound for the potential influence of the dielectric environment on TADF emitters.

Transient absorption spectroscopy of TADF emitters

We have performed transient absorption (TA) spectroscopy on a solution of TXO-TPA in toluene, excited with a 400 nm (100 fs) pulse to populate the ¹CT state (Fig. 2a). 200-300 fs after excitation, we observe two photo-induced absorption (PIA) features: a band in the near-infrared (NIR) peaked at 975 nm and a broad shoulder at 625 nm. Subsequently, a rapid

spectral evolution occurs, with the NIR PIA blue-shifting from 975 nm to 925 nm and the PIA shoulder at 625 nm developing into two new peaks at 520 nm and around 770 nm. We have taken kinetics at wavelengths associated with these features to examine their temporal evolution: the low (1000-1025 nm) and high (920-940 nm) energy edges of the NIR PIA and the shoulder PIA (620-650 nm) (Fig. 2b). We find that the excited state evolutions proceed with a time constant of 6.4 ps (Fig. S2) and are largely complete by 20 ps. This is significantly slower than previous reports of coherent structural changes in organic chromophores after photoexcitation, which take place on hundreds of femtoseconds³²⁻³⁴, suggesting a different origin for these spectral evolutions.

In contrast to TXO-TPA, when exciting 4CzIPN at 400 nm in toluene (Fig. 2e), we notice more subtle spectral shifts; excitation of the lowest energy transition at 450 nm shows the same behaviour, ruling out relaxation from a higher lying state as the cause (Fig. S3). This includes an increase in the intensity of the band centred at 480 nm and a slight red shift in the primary ¹CT PIA at 850 nm, both largely completed within 20 ps (Fig. 2f). We also observe spectral shifts on similar timescales for the other three TADF materials in toluene (Figs. S4-S6), suggesting that it may be an innate part of the TADF process. Calculations of the change in dipole moment in the TADF emitters upon excitation from the ground state to the ¹CT (the absolute dipole moments for these states are given in Table S1) reveal a clear correlation with the magnitude of the spectral shifts (Fig. 1c), with the largest shifts reported for the most dipolar systems (TXO-TPA and DACT-II).

Ultrafast time resolved photoluminescence of TADF emitters

We have investigated the corresponding emissive behaviour with transient grating photoluminescence (TGPL) spectroscopy. We focus here on two TADF materials with contrasting PIA peak shift magnitudes: TXO-TPA and 4CzIPN. In TXO-TPA (Figs. 2c-2d), the emission maximum is 510 nm at 200-300 fs after excitation; significantly higher in energy than the steady-state PL, which peaks at 580 nm (Fig. S1). We then observe a red shift of the emission to 570 nm over identical timescales to the PIA shifts. The picosecond Stokes shift of ~0.3 eV corroborates that the PIA evolutions in the TA result from the environment-mediated stabilization of the ¹CT electronic configuration, consistent with previous observations of solvent-mediated relaxation in materials with CT-type excited states^{23,35-37}. We also observe a large increase in the emission intensity towards 1 ns for the band at 570 nm. We attribute this delayed rise to the emission onset of the fully relaxed ¹CT, in-line with a typical fluorescence rate constant of $\sim 10^7$ s⁻¹ in TADF materials³⁸. There is a concomitant decay in the TXO-TPA ¹CT PIAs over the same timescales (Fig. 2b), confirming the radiative decay of excited states. This delayed rise in the relaxed ¹CT PL, consistent with the small radiative rate expected for a CT-type excitation, also implies that the state responsible for the blue-shifted emission on sub-picosecond timescales has a significantly larger oscillator strength and an increased electron-hole overlap. Therefore, we propose that the dielectric environment drives the formation of a quasi-pure CT excitation in TXO-TPA from an initial state with only partial CT character. Through performing a detailed study on thin films of TXO-TPA dispersed in polystyrene and UGH2 (see SI for details), we find that the picosecond solution spectral shifts in the TA and TGPL in toluene are also present in the solid-state. Thus, we confirm that the solid-state dielectric

environment is also capable of a rapid reorganisation in response to a change in the electronic configuration of the TADF emitter^{13,24,25}, meaning that our findings in solution are also of relevance for the thin films used in OLED devices.

In contrast, there is no significant emission detected from 4CzIPN on early timescales <10 ps (Fig. 2g); instead, as with the fully relaxed ¹CT of TXO-TPA, the luminescence grows in towards 1 ns, with a simultaneous decay in the primary ¹CT PIA kinetic from 870-880 nm beyond 100 ps (Fig. 2f). The delayed onset of emission indicates that after optical excitation, 4CzIPN directly forms a low oscillator strength ¹CT state with a small electron-hole overlap. In addition, we observe no spectral shifts in the 4CzIPN emission on sub-nanosecond timescales, which already matches the steady-state PL (Fig. S7). This signifies that there is minimal delayed electronic or structural evolution induced by the environment in 4CzIPN following excitation to the ¹CT state. These observations are consistent with the limited reorganisation of the surrounding dielectric environment that is expected in response to the small change in the dipole moment of 4CzIPN upon excitation into the ¹CT state.

Impulsive vibrational spectroscopy of TADF emitters

We next probe the nature of the pre- and post-environment reorganization state in TXO-TPA and 4CzIPN with impulsive vibrational spectroscopy (IVS)³⁹. By varying the time between the initial excitation event and the ultrafast pulse that generates vibrational coherences in the excited state, we can probe before (500 fs), during (3 ps), and after (10 ps) the environment-mediated stabilization of the ¹CT. In the spectral range of the ¹CT PIA (790-940 nm) for TXO-TPA, we observe the gradual appearance of two new intense modes at 412 cm⁻¹ and 813 cm⁻¹ (denoted by red asterisks) at 3 and 10 ps that are not present 500 fs after excitation (Fig. 3a). These modes can be considered a fingerprint of the quasi-pure CT product excitation in TXO-TPA and are explored in more detail in the quantum-chemical calculations. In contrast, we do not see the formation of new vibrational modes in the IVS of 4CzIPN, taken over the ¹CT PIA (800-865 nm): only limited changes in the mode intensities (Fig. 3b). The more subtle evolution of the vibrational modes is consistent with the weaker effect of the dielectric environment reorganisation on the molecular and electronic structure of 4CzIPN.

Calculations on the environment dynamics for TXO-TPA

We now discuss the results of the combined quantum mechanics/molecular mechanics (QM/MM) adiabatic dynamics simulations of TXO-TPA in a toluene solution but consider our findings generally applicable to dipolar TADF materials. In the Franck-Condon region, the (vertical) excitation energy to the ¹CT exceeds that of the lowest T₁ (³CT-like) and T₂ (³LE-like) states by 0.4 and 0.1 eV, respectively (Table S2). In the time evolution of the ¹CT excitation energy (Fig. 4a), we observe a complex oscillatory evolution over the whole 10 ps trajectory explored. The presence of a polarized environment with a slow relaxation component is responsible for these large fluctuations in the energy and other observables along the trajectories of the molecular dynamics (MD) simulations. This is because at each time step, the system explores a range of molecular vibrations and solvent degrees of freedom (translational, rotational, and inertial), which results in the emitter experiencing

a different local electric field that modulates its excitation energy through a Stark shift. This effect is not included in the vacuum or PCM models and the large fluctuations are consequently absent from the equivalent simulations, where the molecular co-ordinates of TXO-TPA are shared between the trajectories (Fig. S25). Importantly, these fluctuations are substantial and comparable in magnitude to the singlet-triplet energy gap (E_{ST}). Thus, the ISC and rISC processes could be thought of as being gated by the molecular environment, with crossings occurring when these fluctuations bring the involved states into close energy resonance (*vide infra*). Consistent with the experimental observations, we find that these nuclear motions initially dump ~ 0.3 eV (from ~ 3.1 eV at 0 ps to ~ 2.8 eV at 10 ps) into the environment, also seen in the shift of the ^1CT energy distribution from the early (0-3 ps) to late (3-10 ps) timescales of the explored trajectory (Fig. 4b).

Through analysing the temporal evolution of the electron-hole overlap and the transferred charge in the excited state wavefunction (Fig. S26), we conclude that the decrease in ^1CT energy is associated with an increased CT character of the lowest singlet excited (S_1) state. The increased CT character also manifests in the time evolution of the dihedral angle between the TPA donor and TXO acceptor moieties, which rises from $\sim 50^\circ$ to $\sim 90^\circ$ after 4-5 ps (Fig. 4c). This is reminiscent of twisted intramolecular CT (TICT), where electron transfer from the donor to acceptor involves a change in conformation (rotation around the D-A single bond), and also shows a strong dependence on the dielectric environment⁴⁰. Importantly, this effect is synergistically driven by, but also in response to, solvent polarization effects. One consequence of the ^1CT state acquiring an increasing CT character is a sharp drop in the electron-hole interaction and hence a fall in E_{ST} from the initial ~ 0.4 eV in the ground-state equilibrium geometry down to values as small as ~ 0.1 eV (Fig. 4d). Due to their negligible dipole moment⁴¹, the ^3LE states are only weakly affected by the environment reorganization, remaining at a near-constant energy. As a result, the ^1CT and ^3CT also sweep below the ^3LE (Fig. S27).

To explore the role of the solvent in this process, we have computed the electrostatic potential generated by the toluene molecules over the simulation trajectory (Fig. S28). The results, imaged in Fig. 4e for several snapshots extracted along the *ab initio* MD trajectory, demonstrate how the toluene molecules reorient in response to the dipolar field generated upon photoexcitation of the TXO-TPA solute to the ^1CT state. Here, the yellow and blue colours indicate the positive and negative signs of the electrostatic potential, respectively. These potentials are evaluated based on the point charges associated with the atoms in toluene and reflect the magnitude of the molecular electric dipole moment. Thus, the electrostatic potential directly originates from the molecular dipoles of the toluene solvent molecules. In the ground state, where the molecular dipole moment of TXO-TPA is relatively small, the solvent molecules are randomly distributed around the emitter. Consequently, there is an unstructured electrostatic pattern in the ground-state solvent configuration at 0.3 ps. After excitation of TXO-TPA, the redistribution in the electronic density induces a rearrangement of the surrounding toluene molecules; this solvent orientational response drives the formation of a highly polarized electrostatic environment by 2.5 ps, which further acts back on the electronic structure of the emitter molecule. Together, the concerted solute-solvent effects directly influence the excited state dynamics, causing the picosecond spectroscopic shifts observed experimentally. Importantly,

the collective orientation polarization of the weakly polar toluene molecules is strong enough to lower the TXO-TPA ^1CT excitation energy by ~ 0.3 eV after 10 ps.

Analysis of the vibrational mode evolution for TXO-TPA

To examine the intramolecular reorganization, we have decomposed the predicted spectral dynamics for the ^1CT excitation energies onto the vibrational modes of TXO-TPA as it explores the ^1CT MD trajectory (Fig. 5a), with the molecular localisation of the modes shown in Fig. S29. This provides an instantaneous picture for the modes that contribute the most (those with the highest intensity) to the overall geometric distortion at any given time after excitation. To further visualise this, we have computed the standard deviations of the mode intensities over specific time intervals; this highlights changes in the relative activity of these modes with time (Fig. 5b). By comparing the system at ‘short’ (<3 ps) and ‘long’ (3-10 ps) times after excitation, we find that the interplay of solvent relaxation and geometry-change activates two clusters of molecular vibrational modes at ~ 400 and $\sim 700\text{-}800\text{ cm}^{-1}$, in excellent agreement with the IVS data. The two strongest modes at 417 and 712 cm^{-1} correspond to vibrations extending over both the TPA donor and the TXO acceptor moieties (Fig. S31). We consider that these modes are a fingerprint of the quasi-pure CT excited state, formed after the electronic S_1 state acquires increasing TICT character. Or, in other words, electron transfer occurs adiabatically from TPA to TXO. Relaxation proceeding from this novel non-equilibrium configuration then results in the irreversible formation of the ^1CT product.

Calculations on the triplet state manifold of TXO-TPA

To gain insight into the transient solute-solvent dynamics taking place in the triplet manifold, we have repeated the QM/MM/MD calculations for the lowest adiabatic triplet state; in Fig. 6 we report the results of one 10 ps long MD trajectory. Here, the fluctuations in the environment and molecular vibrations now act in tandem to swap the nature of the lowest energy triplet excitation. This is visualized in Fig. 6a, where for times <5 ps, the time evolution of the electron/hole overlap in the lowest two triplet states exhibits sudden jumps from values as high as ~ 0.8 (indicative of a dominant ^3LE character) to values as low as ~ 0.2 (corresponding to mostly ^3CT excitations).

Between $\sim 5\text{-}6.5$ ps, the lowest energy (and therefore populated) triplet state has a small electron-hole overlap, indicating ^3CT character. Correspondingly, a polarized electrostatic pattern develops in the environment during this metastable time window (Fig. S32). Importantly, the polarized environment that stabilizes the ^3CT also stabilizes the similar orbital nature ^1CT . However, the energy of the ^3LE is not strongly modulated as it possess a much smaller molecular dipole moment²⁰. Thus, S_1 , T_1 and T_2 become simultaneously confined within a narrow energy spacing in the 5-6.5 ps time window of this specific trajectory (Fig. 6b). Critically, this provides the opportunity for population transfer to take place between the singlet and triplet manifolds, which has been shown to occur at the crossing seams of the potential energy surfaces of the states involved⁴². Indeed, the 5-6.5 ps time window in our simulations corresponds to the $S_1\text{-}T_1$ crossing region of Fig. 6d. Furthermore, when the CT-type T_1 state is stabilized for sufficient time, the

same vibrational modes around ~ 400 and $\sim 700\text{-}800\text{ cm}^{-1}$ that were previously observed in the ^1CT manifold are again activated (Fig. 6c). These key modes are able to couple the two spin manifolds, driving triplet-to-singlet conversion⁴³. Thus, we propose that the interplay of solvent and intramolecular reorganization, seen in our trajectories as stochastic environmental fluctuations, gives rise to quasi-equilibrium conditions that are favourable for rISC to take place. This suggests the rISC process in dipolar TADF emitters is directly gated by the dielectric environment.

Effect of environment dynamics on the rISC rate

To quantify the contribution of the dielectric environment to ISC and rISC in TXO-TPA, we have transformed 25 ps of singlet and 30 ps of triplet trajectories for both an explicit toluene solvent and a vacuum environment (Fig. S34) into reactant and product free energy functions, $g_a(X)$ (see Methods for details), using the $S_1\text{-}T_1$ energy gap as generalized microscopic reaction coordinate (Figs. 6d-6e)⁴⁴. From the free energy curves, we extract a mean reorganisation energy (λ) of 210 meV and $G^0=95$ meV for TXO-TPA in the explicit toluene solvent, corresponding to an activation energy (E_A) of ~ 15 meV for ISC and ~ 110 meV for rISC. In contrast, we obtain $\lambda=750$ meV and $G^0=140$ meV for TXO-TPA in vacuum; this translates into a significantly higher E_A of ~ 124 meV for ISC and ~ 264 meV for rISC.

To examine the impact of the dielectric environment on the rate of ISC (k_{ISC}) and rISC (k_{rISC}), we input the values obtained from our free energy functions into a classical Marcus-type non-adiabatic expression⁴², taking a conservative estimate for the SOC of 0.5 cm^{-1} from our simulations (Fig. S33). From this, we obtain $k_{ISC}=7.6\times 10^7\text{ s}^{-1}$ and $k_{rISC}=1.8\times 10^6\text{ s}^{-1}$ for the explicit toluene and $k_{ISC}=6.0\times 10^5\text{ s}^{-1}$ and $k_{rISC}=2.5\times 10^3\text{ s}^{-1}$ for the vacuum environment. The calculated rates for TXO-TPA in toluene are already in good agreement with experiment ($k_{ISC}=5.7\times 10^7\text{ s}^{-1}$ and $k_{rISC}=2.3\times 10^5\text{ s}^{-1}$) but can be further improved by using a semi-classical Marcus-Levich-Jortner expression with one vibrational mode treated quantum mechanically (either the ~ 400 or $\sim 800\text{ cm}^{-1}$ modes identified for TXO-TPA; Fig. S35)⁴⁵. Thus, even a weakly polar dielectric environment, such as toluene, makes a significant contribution to the rISC (and ISC) rates in a dipolar TADF emitter.

Conclusions

In this work, we have demonstrated that the stochastic dielectric environment dynamics can directly gate the ISC and rISC processes in TADF emitters. Consequently, even a weakly polar environment like a toluene solution can significantly reduce the activation energy for rISC in a dipolar emitter, such as TXO-TPA, effectively increasing k_{rISC} by up to three orders of magnitude when compared to the isolated molecule. Furthermore, our experimental results suggest that dipolar TADF molecules exhibit similar behaviour in thin films, meaning the dielectric environment effects seen in solution are also of relevance to OLED devices. In contrast, the dielectric environment plays a more limited role in a less dipolar multi-D TADF emitter, 4CzIPN. Thus, we predict that the dielectric environment dynamics will have a much smaller impact on the rISC activation energy in 4CzIPN and therefore a limited influence on the rISC rate. Consequently, we propose that tuning the

dielectric environment is likely to be a powerful tool for controlling rISC in dipolar TADF emitters, including many materials with D-A or D-A-D structural motifs. However, other approaches are likely to be more beneficial for manipulating the rISC rate in multi-D systems that show a smaller change in their dipole moment upon excitation.

Methods

Transient Absorption

Transient absorption (TA) measurements were performed on a home-built TA setup, powered by a Ti:sapphire amplifier (Spectra Physics Solstice Ace) that generated 100 fs duration pulses centred at 800 nm, with a repetition rate of 1 kHz. On this setup, sample photoexcitation in the short-time TA experiments (100 fs-1.7 ns) was achieved by the second harmonic (400 nm) of the 800 nm output of the Ti:sapphire amplifier, generated using a β -Barium Borate (BBO) crystal and filtered with a 3 mm thick BG39 glass filter to remove the residual 800 nm fundamental pulse. The probe light was generated by home-built broadband visible (500-770 nm) and near-infrared (830-1025 nm) non-collinear optical parametric amplifiers (NOPAs), pumped using the 400 nm second harmonic of the Ti:sapphire output. For short-time measurements, a mechanical delay stage (Thorlabs DDS300-E/M) was used provide the pump-probe delay. In the long-time measurements, the delay between probe and pump pulses was varied using a Stanford DG645 delay generator. The transmitted probe pulses were collected with a silicon dual-line array detector (Hamamatsu S8381-1024Q) which was driven and read out by a custom-built board from Stresing Entwicklungsbüro.

Transient Grating Photoluminescence

A Ti:Sapphire amplifier system (Spectra Physics Solstice Ace) operating at 1 kHz generating 100 fs pulses was split into the pump and probe beam arms. The pump beam was generated by second harmonic generation (SHG) in a BBO crystal and focused onto the sample. The photoluminescence generated is collimated using a silver off-axis parabolic mirror and focused onto the gate medium. About 80 μ J/pulse of the 800 nm laser output is used for the gate beams, which is first raised 25 mm above the plane of the PL to produce a boxcar geometry and split into a pair of gate beams using a 50/50 beam splitter. The gate beams are focused onto the gate medium (fused silica), crossing at an angle of $\sim 5^\circ$ and overlapping with the focused PL. The two gate beams interfere and create a transient grating in the gate medium due to a modulation of the refractive index via the optical Kerr effect. Temporal overlap between the two gate beams is achieved via a manual delay stage. The PL is then deflected on the transient grating causing a spatial separation of the gated signal from the PL background. Two lenses collimate and focus the gated signal onto the spectrometer entrance (Princeton Instruments SP 2150) after long- and short-pass filters remove scattered pump and gate light, respectively. Gated PL spectra are measured using an intensified CCD camera (Princeton Instruments, PIMAX4). The (~ 10 ns) electronic shutter of the intensified CCD camera was used to further suppress long-lived PL background. PL spectra at each gate time delay are acquired from ~ 10000 laser shots. The time delay between pump and gate beams is controlled via a motorized optical delay line on the excitation beam path and a LabVIEW data acquisition program.

ns- μ s Transient Photoluminescence

Transient PL spectra were recorded using an electrically gated intensified charge-coupled device (ICCD) camera (Andor iStar DH740 CCI-010) connected to a calibrated grating spectrometer (Andor SR303i). Pulsed 400 nm photoexcitation was provided at a repetition rate of 1 kHz. A 425 nm long-pass filter (Edmund Optics) was used to prevent scattered laser signal from entering the camera. Temporal evolution of the PL emission was obtained by stepping the ICCD gate delay with respect to the excitation pulse. The minimum gate width of the ICCD was 5 ns. Recorded data was subsequently corrected to account for filter transmission and camera sensitivity.

Impulsive Vibrational Spectroscopy

The IVS experiments were performed using a Yb:KGW laser system (Pharos, Light Conversion) to provide 15.2 W at 1030 nm with a 38 kHz repetition rate. The probe beam was generated by focusing a portion of the fundamental in a 4 mm YAG crystal to generate a white light continuum (WLC). The push beam was generated by a non-collinear optical parametric amplifier (NOPA) seeded by the WLC from a 3 mm YAG crystal mixed with a second harmonic pump (HIRO, Light Conversion) in a barium borate crystal (23.5° cut, type I phase matching, ~2° external angle). The NOPA output was compressed down to <10 fs pulses using a pair of chirped mirrors and pair of CaF₂ wedges, as determined by second-harmonic generation frequency-resolved optical gating (SHG-FROG) During the measurement, the push pulse intensity was kept low enough to avoid detectable two-photon absorption. The pump was generated using a narrow band optical parametric oscillator system (ORPHEUS-LYRA, Light conversion) with a 1030 nm seed. The FWHM of the pump was ~200 fs. The probe white light was delayed using a computer-controlled piezoelectric translation stage (Physik Instrumente). The pump was delayed using a computer controlled Thorlabs translation stage. The pulse train of probe pulses with/without the pump and with/without the push was generated using separate chopper wheels on the pump and push beams. After the sample, the probe pulse was split with a 950 nm dichroic mirror (Thorlabs). The visible part was then imaged with a Silicon photodiode array camera (Stresing Entwicklunsbüro; visible monochromator 550 nm blazed grating). The near-infrared portion of the probe was focused into to an IR spectrograph (1200 nm blazed grating) and imaged on an InGaAs photodiode array camera (Sensors Unlimited). Offsets for the differing spectral response of the detectors was accounted for in the post-processing of data.

4CzIPN was excited with a 450 nm (200 fs) pump pulse to populate the ¹CT electronic state directly. Owing to its weaker ¹CT absorption band, TXO-TPA was instead excited with a 343 nm (270 fs) pump pulse. Importantly, the observed behaviour of TXO-TPA excited at 343 nm is equivalent to excitation at 400 nm, with all spectral evolutions again completed by 20 ps (Fig. S16). Subsequently, a second ultrafast (<10 fs; shorter than the period of most vibrational modes) ‘push’ pulse, resonant with the ¹CT PIA, was used to generate vibrational coherences in the molecular normal modes of the ¹CT potential energy surface. We note that it is not possible to reliably individually resolve very low frequency modes (<100 cm⁻¹) due to their extremely long oscillation periods, which can extend beyond the lifetime of the picosecond coherences generated in the IVS experiment. To resolve the

excited state vibrational modes from the ground state modes, IVS requires a large fraction (~1-10%) of the molecules under investigation to be excited. This necessitates the use of very high excitation fluences, which can lead to rapid material degradation in solid films. Thus, we have focussed on the toluene solutions in our work.

Fast Fourier transforming the femtosecond-transient absorption data allows determination of the mode frequency modulating the electronic transition. Briefly, each row of the TA data, y , contains kinetic information at wavelength i , and is fitted with a multiple exponential decay functions.

$$y_i = \sum_n \frac{1}{2} \cdot A_n \cdot e^{\frac{s^2}{2\tau n^2}} \cdot e^{-\frac{(t-t_0)}{\tau_n}} \cdot \left(1 + \operatorname{erf} \left(\frac{t-t_0 - \frac{s^2}{\tau_n}}{\sqrt{2}s} \right) \right) \quad (1)$$

The n lifetimes, τ , are treated as a common fitting parameter for the whole data set, each with a different weighting A_n at a particular wavelength. A chirp and background correction were performed before the global fit.

$$y_i = \sum_n \frac{1}{2} \cdot A_n \cdot e^{\frac{s^2}{2\tau n^2}} \cdot e^{-\frac{(t-t_0)}{\tau_n}} \cdot \left(1 + \operatorname{erf} \left(\frac{t-t_0 - \frac{s^2}{\tau_n}}{\sqrt{2}s} \right) \right) \quad (2)$$

The error function considers the Gaussian-shaped probe pulse arriving at $t = t_0$ and instrumental response time, s . The TA data can be modelled as a matrix multiplication in the form of

$$\mathbf{y} = \mathbf{A} \cdot \mathbf{E} = \begin{pmatrix} A_{11} & \cdots & A_{1n} \\ \vdots & \ddots & \vdots \\ A_{m1} & \cdots & A_{mn} \end{pmatrix} \cdot \begin{pmatrix} E_{11} & \cdots & E_{1t} \\ \vdots & \ddots & \vdots \\ E_{n1} & \cdots & E_{nt} \end{pmatrix} \quad (3)$$

where m , n and t are the number of wavelengths, lifetimes and timepoints in the data. \mathbf{E} is a matrix containing all the exponential components in Equation 2 and \mathbf{A} can be computed by a simple matrix division provided we have initial guesses for the various parameters. τ , t_0 and s were then fitted iteratively, and \mathbf{A} updated after each iteration, until convergence was achieved.

A Blackman window was then applied to the residual map before Fast Fourier Transform was performed on the linear time region. The data was padded with zero arrays to improve FFT performance.

Steady-state absorption

Steady-state absorption spectra were measured using an HP 8453 spectrometer.

Steady-state photoluminescence

The steady-state PL was measured in an integrating sphere, where the samples were excited with a 405 nm continuous-wave laser. The emission signals were measured using a calibrated Andor iDus DU420A BVF Si detector.

Photoluminescence quantum efficiency measurements

The PLQE was determined using method previously described by De Mello *et al.*⁴⁶. Samples were placed in an integrating sphere and photoexcited using a 405 nm continuous-wave laser. The laser and emission signals were measured and quantified using a calibrated Andor iDus DU420A BVF Si detector.

Raman spectroscopy

Raman spectroscopy measurements were performed on films fabricated on a quartz substrate. The Raman spectra were collected using a HORIBA T64000 Raman spectrometer attached to a confocal microscope with a 100× objective and a 633 nm laser for the excitation. Laser power was minimized to ensure that no degradation of the sample was induced. The spectra were averaged over several accumulations.

Computational details

The changes in dipole moment upon a vertical excitation to the lowest singlet state were calculated at the density functional theory (DFT) level using the PBEh-3c functional⁴⁷, implemented in ORCA software⁴⁸. To study the time-evolution of the singlet and triplet states, our computational modelling uses a combined QM/MM approach. For these investigations, a single TXO-TPA molecule was surrounded by 249 individual toluene molecules and the reorganization dynamics following population of the ¹CT and ³CT states were determined. This was achieved by employing an electrostatic embedding scheme, where interaction with the solvent includes the electronic polarization of the QM TXO-TPA molecule by re-orientation of the MM toluene molecules, together with Lennard-Jones potentials. Thus, this approach accounts for the (slow) inertial component of the solvent dielectric response, whilst the optical component that produces an instantaneous and rigid shift of the transition energies is ignored⁴⁹. The TXO-TPA molecule was described at the DFT level, while the surrounding 249 toluene molecules were treated with the GROMOS 54a7 classical force field⁵⁰ in Gomacs code⁵¹. We explored the adiabatic excited-state dynamics in the ¹CT for the first 10 ps using the forces from time-dependent (TD)-DFT. The same approach was further utilized to study the triplet dynamics, sampling the geometries from 10 ps of adiabatic dynamics in the lowest triplet state from open-shell DFT calculations, before applying spin-adapted TD-DFT calculations to access the properties of higher-lying triplet excitons. The electron and hole densities of the three lowest energy triplet states (T_1 , T_2 and T_3), calculated in the gas-phase ground-state equilibrium geometry of TXO-TPA, are displayed in Fig. S24. We note that whilst T_2 and T_3 are ³LE states localized on the TXO moiety, T_1 has primarily ³CT character. Finally, to quantify the extension of the normal modes along the molecular backbone, we defined the participation ratio as $PR(D/A) = \sum \Delta_{D/A}^2 / \sum \Delta^2$, where Δ is a Cartesian displacement for each atom. Further computational details are provided in SI.

To generate the free energy curves for the singlet and triplet manifolds in Figs. 6d and 6e, we have transformed 25 ps of singlet and 30 ps of triplet trajectories for both an explicit toluene solvent and a vacuum environment (trajectories in Fig. S34) into reactant and product free energy functions, $g_a(X)$, using the S_1 - T_1 energy gap as generalized microscopic reaction coordinate (Figs. 7a and 7b)⁴⁴. For the reactant, this is given by:

$$\Delta g_a(X) = -kT \ln[P(X)_a] \quad \# \quad (4)$$

where $(X)_a = E_\beta - E_a$, with a denoting the reactant and β the product; and $P(X)_a$ is the probability that the system will have a given value of X along the trajectories propagated on state a . Thus, $a \equiv S_1$ and $\beta \equiv T_1$ for the singlet trajectories; a similar free energy function can be obtained for the product, ($a \equiv T_1$ and $\beta \equiv S_1$) from the triplet trajectories, now adding the reaction free energy, G^0 , to Eq. 1. Here, it is important to note that the free energy function for the triplet is that of the lowest adiabatic T_1 state, which involves a dynamically evolving mixture of 3CT and 3LE excitations (Fig. 6a). In effect, the functions of $g_a(X)$ are the microscopic equivalents of the Marcus parabola, where the minima represent the most frequently encountered S_1 - T_1 energy gap in the trajectories; a free energy gain is required to move away from the minima, as expected for less commonly occurring S_1 - T_1 gaps. Differently to Aizawa *et al.*⁴², we note the appearance of a crossing seam between S_1 and T_1 (at $X = 0$, by definition of the free energy functions) as these involve (slightly) different electronic configurations with sufficient SOC to drive rISC.

Supplementary Material

Refer to Web version on PubMed Central for supplementary material.

Acknowledgements

A.J.G. and R.H.F. acknowledge support from the Simons Foundation (grant no. 601946) and the EPSRC (EP/M01083X/1 and EP/M005143/1). This project has received funding from the European Research Council (ERC) under the European Union's Horizon 2020 research and innovation programme (R.H.F. grant agreement No. 670405 and A.R. grant agreement No. 758826). A.R. thanks the Winton Programme for the Physics of Sustainability for funding. A.P., Y.O. and D.B. were supported by the European Union's Horizon 2020 research and innovation programme under Marie Skłodowska Curie Grant agreement 748042 (MILORD project). Computational resources in Mons were provided by the Consortium des Équipements de Calcul Intensif (CÉCI), funded by the Fonds de la Recherche Scientifiques de Belgique (F.R.S.-FNRS) under Grant No. 2.5020.11, as well as the Tier-1 supercomputer of the Fédération Wallonie-Bruxelles, infrastructure funded by the Walloon Region under Grant Agreement No. 1117545. D.B. is a FNRS Research Director. R.P. acknowledges financial support from an EPSRC Doctoral Prize Fellowship. A.J.S. acknowledges the Royal Society Te Apārangi and the Cambridge Commonwealth European and International Trust for their financial support. Y.O. acknowledges funding by the Fonds de la Recherche Scientifique-FNRS under Grant no. F.4534.21 (MIS-IMAGINE). L.-S.C. acknowledges funding from the USTC Research Funds of the Double First-Class Initiative and the National Natural Science Foundation of China (NSFC) (grant no. 52103242) and this work was partially carried out at the USTC Center for Micro and Nanoscale Research and Fabrication. We thank C. Schnedermann for useful discussions.

Data availability

The data that supports the plots within this paper is available at the University of Cambridge Repository: <https://doi.org/10.17863/CAM.85068>.

References

1. Uoyama H, Goushi K, Shizu K, Nomura H, Adachi C. *Nature*. 2012; 492: 234–238. [PubMed: 23235877]
2. Zhang Q, Li B, Huang S, Nomura H, Tanaka H, Adachi C. *Nat Photonics*. 2014; 8: 326–332.
3. Lin T-A, Chatterjee T, Tsai W-L, Lee W-K, Wu M-J, Jiao M, Pan K-C, Yi C-L, Chung C-L, Wong K-T, Wu C-C. *Adv Mater*. 2016; 28: 6976–6983. [PubMed: 27271917]
4. Czerwieńiec R, Yu J, Yersin H. *Inorg Chem*. 2011; 50: 8293–8301. [PubMed: 21812428]
5. Dias FB, Bourdakos KN, Jankus V, Moss KC, Kamtekar KT, Bhalla V, Santos J, Bryce MR, Monkman AP. *Adv Mater*. 2013; 25: 3707–3714. [PubMed: 23703877]
6. Liu Y, Li C, Ren Z, Yan S, Bryce MR. *Nat Rev Mater*. 2018; 3: 18020
7. Wu T-L, Huang M-J, Lin C-C, Huang P-Y, Chou T-Y, Chen-Cheng R-W, Lin H-W, Liu R-S, Cheng C-H. *Nat Photonics*. 2018; 12: 235–240.
8. Etherington MK, Gibson J, Higginbotham HF, Penfold TJ, Monkman AP. *Nat Commun*. 2016; 7: 13680 [PubMed: 27901046]
9. Gibson J, Monkman AP, Penfold TJ. *ChemPhysChem*. 2016; 17: 2956–2961. [PubMed: 27338655]
10. Noda H, Chen X-K, Nakanotani H, Hosokai T, Miyajima M, Notsuka N, Kashima Y, Brédas J-L, Adachi C. *Nat Mater*. 2019; 18: 1084–1090. [PubMed: 31477903]
11. Drummond BH, Aizawa N, Zhang Y, Myers WK, Xiong Y, Cooper MW, Barlow S, Gu Q, Weiss LR, Gillett AJ, Credgington D, et al. *Nat Commun*. 2021; 12: 4532. [PubMed: 34312394]
12. dos Santos PL, Ward JS, Bryce MR, Monkman AP. *J Phys Chem Lett*. 2016; 7: 3341–3346. [PubMed: 27505620]
13. Deng C, Zhang L, Wang D, Tsuboi T, Zhang Q. *Adv Opt Mater*. 2019; 7: 1801644
14. Méhes G, Goushi K, Potscavage WJ, Adachi C. *Org Electron*. 2014; 15: 2027–2037.
15. Olivier Y, Yurash B, Muccioli L, D'Avino G, Mikhnenko O, Sancho-García JC, Adachi C, Nguyen T-Q, Beljonne D. *Phys Rev Mater*. 2017; 1: 075602
16. Yersin H, Mataranga-Popa L, Czerwieńiec R, Dovbii Y. *Chem Mater*. 2019; 31: 6110–6116.
17. Hosokai T, Noda H, Nakanotani H, Nawata T, Nakayama Y, Matsuzaki H, Adachi C. *J Photonics Energy*. 2018; 8: 1.
18. Han C, Zhang Z, Ding D, Xu H. *Chem*. 2018; 4: 2154–2167.
19. Parusel A. *J Chem Soc Faraday Trans*. 1998; 94: 2923–2927.
20. Northey T, Stacey J, Penfold TJ. *J Mater Chem C*. 2017; 5: 11001–11009.
21. Cui L-S, Gillett AJ, Zhang S-F, Ye H, Liu Y, Chen X-K, Lin Z-S, Evans EW, Myers WK, Ronson TK, Nakanotani H, et al. *Nat Photonics*. 2020; 14: 636–642.
22. Tang X, Cui L-S, Li H-C, Gillett AJ, Auras F, Qu Y-K, Zhong C, Jones STE, Jiang Z-Q, Friend RH, Liao L-S. *Nat Mater*. 2020; 19: 1332–1338. [PubMed: 32541938]
23. Kuang Z, He G, Song H, Wang X, Hu Z, Sun H, Wan Y, Guo Q, Xia A. *J Phys Chem C*. 2018; 122: 3727–3737.
24. Delor M, McCarthy DG, Cotts BL, Roberts TD, Noriega R, Devore DD, Mukhopadhyay S, De Vries TS, Ginsberg NS. *J Phys Chem Lett*. 2017; 8: 4183–4190. [PubMed: 28829138]
25. Cotts BL, McCarthy DG, Noriega R, Penwell SB, Delor M, Devore DD, Mukhopadhyay S, De Vries TS, Ginsberg NS. *ACS Energy Lett*. 2017; 2: 1526–1533.
26. Wang H, Xie L, Peng Q, Meng L, Wang Y, Yi Y, Wang P. *Adv Mater*. 2014; 26: 5198–5204. [PubMed: 24903266]
27. Kaji H, Suzuki H, Fukushima T, Shizu K, Suzuki K, Kubo S, Komino T, Oiwa H, Suzuki F, Wakamiya A, Murata Y, et al. *Nat Commun*. 2015; 6: 8476 [PubMed: 26477390]
28. Noguchi Y, Miyazaki Y, Tanaka Y, Sato N, Nakayama Y, Schmidt TD, Brütting W, Ishii H. *J Appl Phys*. 2012; 111: 114508
29. Ritzoulis G, Papadopoulos N, Jannakoudakis D. *J Chem Eng Data*. 1986; 31: 146–148.
30. Yu S, Hing P, Hu X. *J Appl Phys*. 2000; 88: 398–404.
31. Skuodis E, Bezvikonny O, Tomkeviciene A, Volyniuk D, Mimaite V, Lazauskas A, Bucinskas A, Keruckiene R, Sini G, Grazulevicius JV. *Org Electron*. 2018; 63: 29–40.

32. Takeuchi S, Ruhman S, Tsuneda T, Chiba M, Taketsugu T, Tahara T. *Science* (80-). 2008; 322: 1073–1077.
33. Iwamura M, Watanabe H, Ishii K, Takeuchi S, Tahara T. *J Am Chem Soc.* 2011; 133: 7728–7736. [PubMed: 21524124]
34. Iwamura M, Takeuchi S, Tahara T. *Acc Chem Res.* 2015; 48: 782–791. [PubMed: 25646861]
35. Karunakaran V, Das S. *J Phys Chem B.* 2016; 120: 7016–7023. [PubMed: 27347705]
36. Choi J, Ahn D-S, Oang KY, Cho DW, Ihee H. *J Phys Chem C.* 2017; 121: 24317–24323.
37. Petrozza A, Laquai F, Howard IA, Kim J-S, Friend RH. *Phys Rev B.* 2010; 81: 205421
38. Hosokai T, Matsuzaki H, Nakanotani H, Tokumaru K, Tsutsui T, Furube A, Nasu K, Nomura H, Yahiro M, Adachi C. *Sci Adv.* 2017; 3 e1603282 [PubMed: 28508081]
39. Liebel M, Kukura P. *J Phys Chem Lett.* 2013; 4: 1358–1364. [PubMed: 26282153]
40. Sasaki S, Drummen GPC, Konishi GI. *J Mater Chem C.* 2016; 4: 2731–2743.
41. Santos PL, Ward JS, Data P, Batsanov AS, Bryce MR, Dias FB, Monkman AP. *J Mater Chem C.* 2016; 4: 3815–3824.
42. Aizawa N, Harabuchi Y, Maeda S, Pu Y-J. *Nat Commun.* 2020; 11: 3909. [PubMed: 32764588]
43. Niu Y, Peng Q, Shuai Z. *Sci China Ser B Chem.* 2008; 51: 1153–1158.
44. Warshel A, Parson WW. *Annu Rev Phys Chem.* 1991; 42: 279–309. [PubMed: 1747189]
45. Samanta PK, Kim D, Coropceanu V, Brédas J-L. *J Am Chem Soc.* 2017; 139: 4042–4051. [PubMed: 28244314]
46. de Mello JC, Wittmann HF, Friend RH. *Adv Mater.* 1997; 9: 230–232.
47. Grimme S, Brandenburg JG, Bannwarth C, Hansen A. *J Chem Phys.* 2015; 143: 054107 [PubMed: 26254642]
48. Neese F. *WIREs Comput Mol Sci.* 2018; 8: 4–9.
49. Dhali R, Phan Huu DKA, Terenziani F, Sissa C, Painelli A. *J Chem Phys.* 2021; 154: 134112 [PubMed: 33832272]
50. Schmid N, Eichenberger AP, Choutko A, Riniker S, Winger M, Mark AE, van Gunsteren WF. *Eur Biophys J.* 2011; 40: 843–856. [PubMed: 21533652]
51. Berendsen HJC, van der Spoel D, van Drunen R. *Comput Phys Commun.* 1995; 91: 43–56.

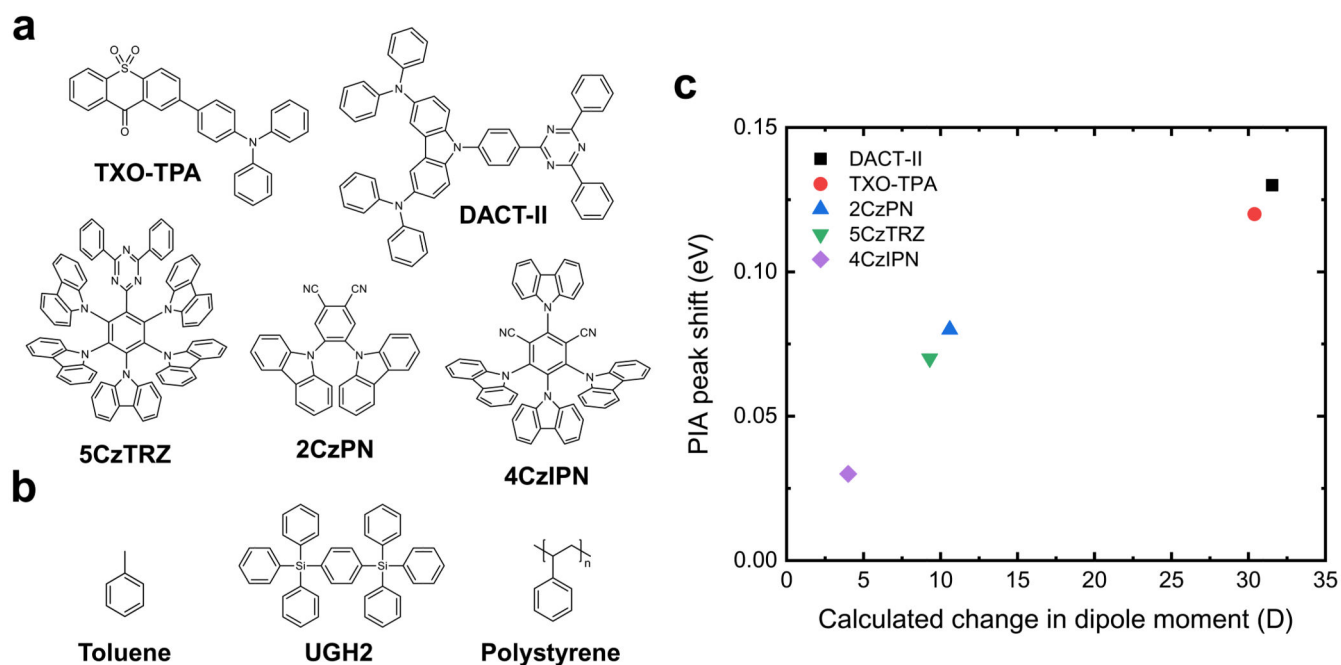


Figure 1. Chemical structures and change in dipole moment upon excitation for the investigated TADF emitters.

(a) The chemical structures of the five TADF emitters investigated in this study. The emitters were chosen to provide a representative selection of the popular structural motifs employed in high-performance TADF materials. This includes linear donor-acceptor (D-A; TXO-TPA and DACT-II), D-A-D (2CzPN) and multi-D (4CzIPN and 5CzTRZ). (b) The chemical structures of the host materials investigated in this study, chosen to represent solution (toluene), small molecule (UGH-2) and polymer (polystyrene). (c) The measured shift in the ¹CT photo-induced absorption (PIA) peak between 0.3 and 100 ps (in eV) as a function of the calculated change in the dipole moment of the emitter upon excitation from the ground state to the ¹CT state. In 2CzPN where more than one ¹CT PIA is present, the PIA with the largest energy shift is presented.

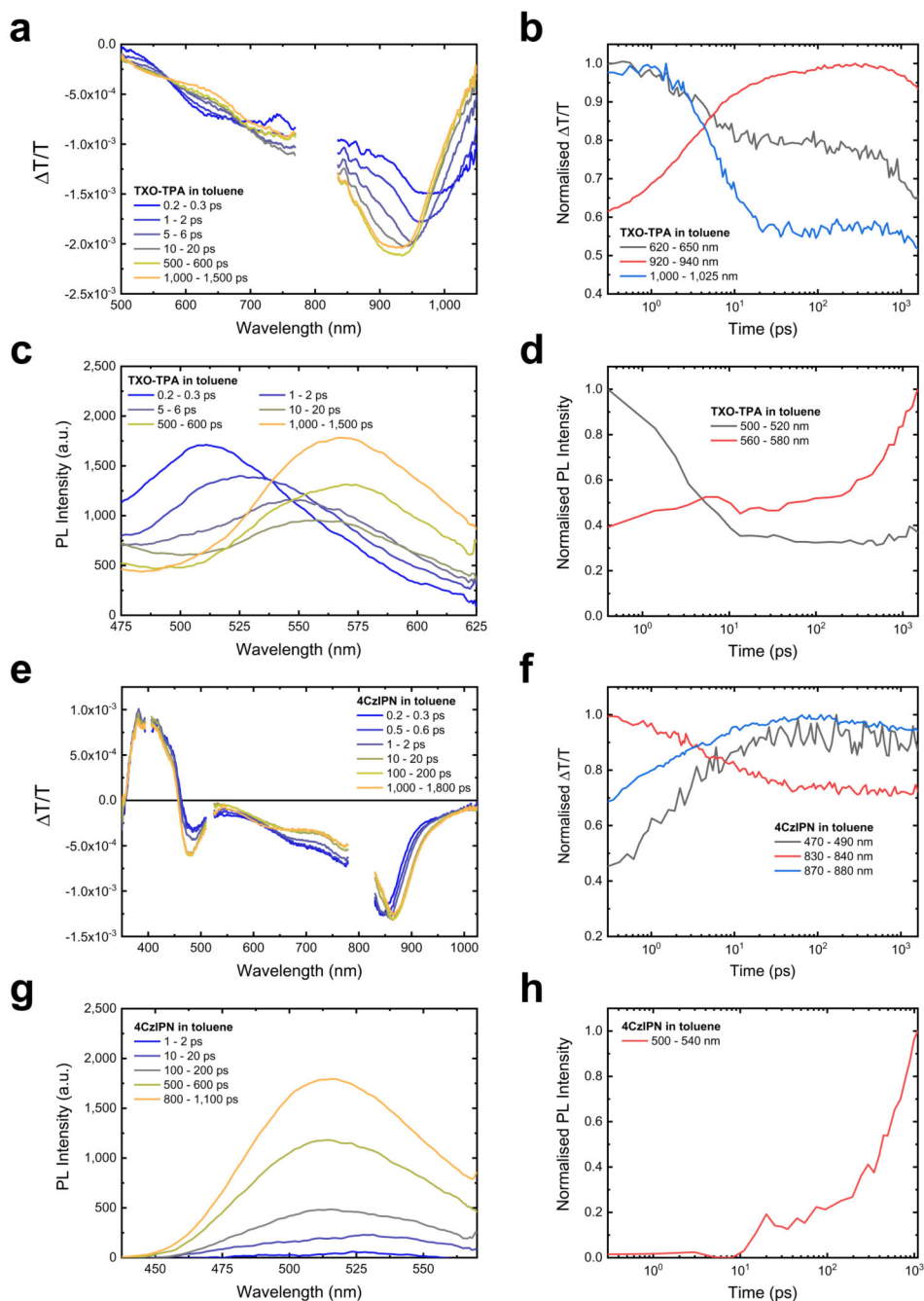


Figure 2. Ultrafast transient absorption and photoluminescence measurements of TXO-TPA and 4CzIPN in toluene solutions.

(a) The TA spectra of TXO-TPA in an oxygen-free toluene solution, excited at 400 nm with a fluence of $15.6 \mu\text{J}/\text{cm}^2$. (b) The TA kinetics of TXO-TPA in toluene, taken from the SE region (620-650 nm), the high energy edge of the ^1CT PIA (920-940 nm) and the low energy edge of the ^1CT PIA (1000-1025 nm). (c) The TGPL spectra of TXO-TPA in a toluene solution, excited at 400 nm with a fluence of $50.9 \mu\text{J}/\text{cm}^2$. (d) The kinetics of the TGPL, taken at the high energy (500-520 nm) and low energy (560-580 nm) edges of the TXO-TPA

PL. **(e)** The TA spectra of 4CzIPN in an oxygen-free toluene solution, excited at 400 nm with a fluence of $28.3 \mu\text{J}/\text{cm}^2$. **(f)** The TA kinetics of 4CzIPN in toluene, taken from the highest energy PIA (470-490 nm), the high energy edge of the ^1CT PIA (830-840 nm) and the low energy edge of the ^1CT PIA (870-880 nm). **(g)** The TGPL spectra of 4CzIPN in a toluene solution, excited at 400 nm with a fluence of $50.9 \mu\text{J}/\text{cm}^2$. **(h)** The kinetics of the TGPL, taken around the peak of the 4CzIPN PL (500-540 nm).

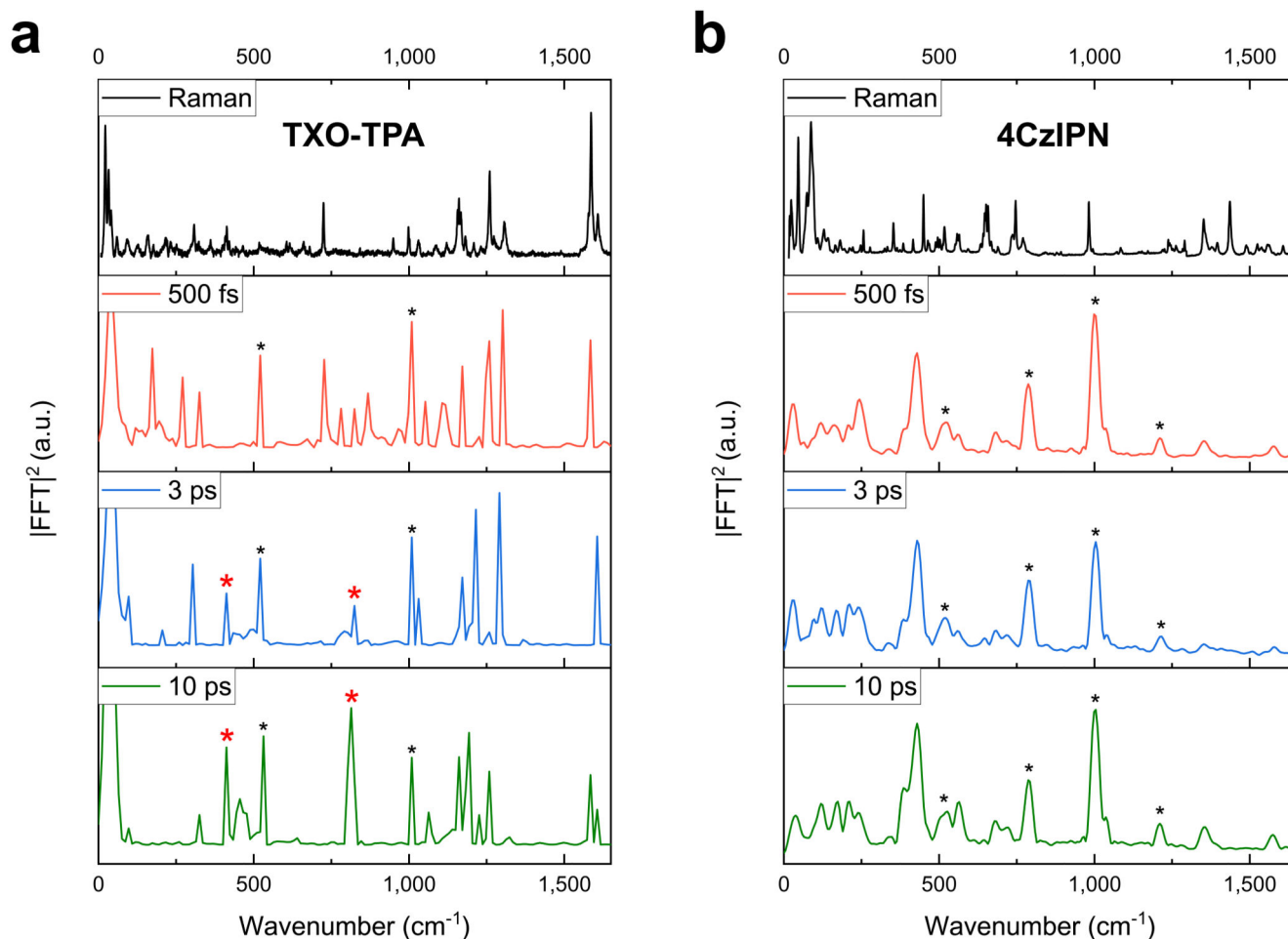


Figure 3. Impulsive vibrational spectroscopy of TXO-TPA and 4CzIPN in toluene solutions. (a) The IVS and steady-state Raman of TXO-TPA. The top panel displays the steady state off resonant (633 nm) Raman spectra of a neat TXO-TPA film. This can be compared to the IVS spectra of TXO-TPA in toluene taken at 0.5, 3 and 10 ps after excitation to isolate the modes that are associated with the ^1CT excited state of TXO-TPA; the key modes associated with the formation of the quasi-pure CT state at 412 and 813 cm^{-1} are denoted by red asterisks (toluene solvent modes are marked by black asterisks). The IVS was obtained by first exciting TXO-TPA at 343 nm with a 270 fs pulse (fluence 0.75 mJ/cm^2), before a second pulse centered at 790 nm with a 9.8 fs duration was used (1.1 mJ/cm^2) to induce coherent oscillations in the excited state of TXO-TPA. (b) The IVS and steady-state Raman spectra of 4CzIPN. The top panel displays the steady state off resonant (633 nm) Raman spectra of a neat 4CzIPN film. This can be compared to the IVS spectra of 4CzIPN in toluene taken at 0.5, 3 and 10 ps after excitation to isolate the modes that are associated with the ^1CT excited state of 4CzIPN. Toluene solvent modes are marked by black asterisks. The IVS was obtained by first exciting 4CzIPN at 450 nm with a 200 fs pulse (fluence 0.47 mJ/cm^2), before a second pulse at 850 nm with a 8.5 fs duration was used (5.7 mJ/cm^2) to induce coherent oscillations in the excited state of 4CzIPN.

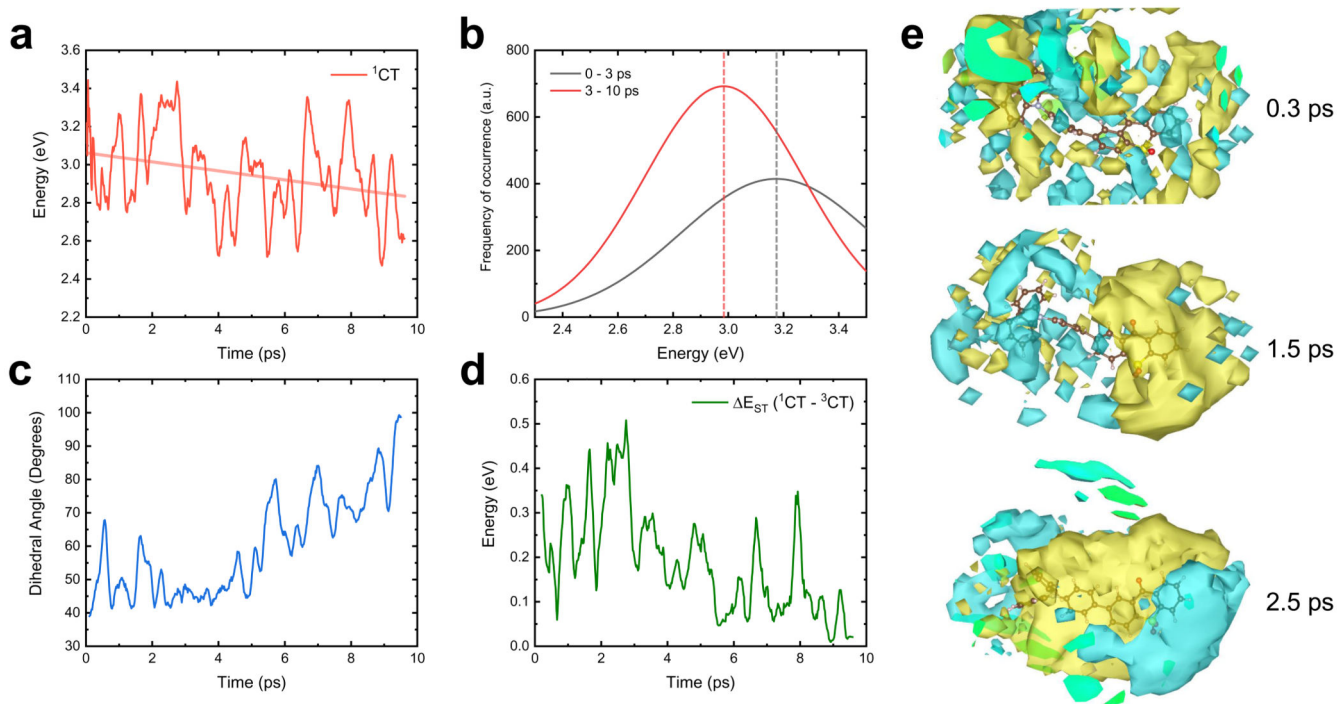


Figure 4. Quantum chemical calculations on TXO-TPA in a toluene solvent.

(a) The vertical excitation energy of the ^1CT state along the simulation trajectory. The overlaid line is a linear best-fit guide to the eye. (b) The distribution of the vertical ^1CT excitation energies during early (0-3 ps) and late (3-10 ps) sections of the simulation trajectory. The dotted lines overlaid mark the peak of the ^1CT energy distribution, showing that the average energy of the ^1CT state decreases due to the environment reorganisation. (c) The evolution of the D:A dihedral angle over the simulation trajectory. The dihedral angle increases from $\sim 50^\circ$ to $\sim 90^\circ$ after 4-5 ps, indicating the formation of a TICT state. (d) The E_{ST} between the ^1CT and ^3CT states along the simulation trajectory. (e) A visualisation of the electrostatic potential of the solvent experienced by TXO-TPA at the indicated timescales of the trajectory. The yellow and blue colours indicate the positive and negative signs of the electrostatic potential, respectively. By 2.5 ps, the toluene molecules surrounding TXO-TPA are strongly polarised in response to the optical formation of the highly dipolar ^1CT state.

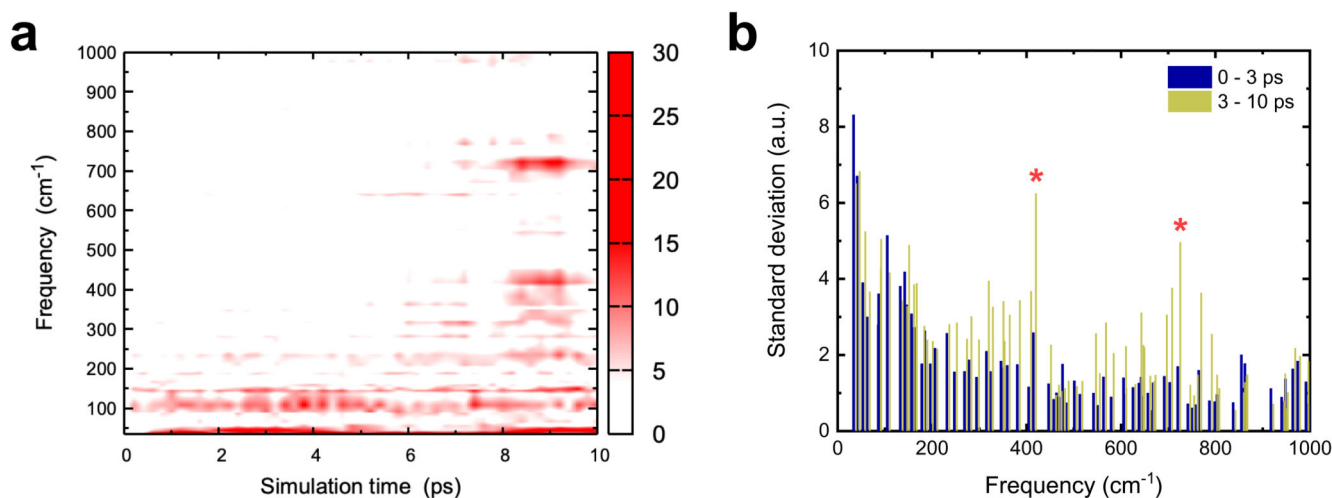


Figure 5. The calculated vibrational mode evolution of TXO-TPA in a toluene solvent. (a) The time evolution of the normal modes along the ¹CT adiabatic dynamics. The colour scale indicates the mode intensity. (b) The standard deviations of the mode intensities computed during the early (0-3 ps) and late (3-10 ps) simulation timescales. Over the later timescales where the solvent has reorganised to drive the formation of a quasi-pure CT state, the modes at 417 and 712 cm⁻¹ become strongly active (as denoted by the red asterisks).

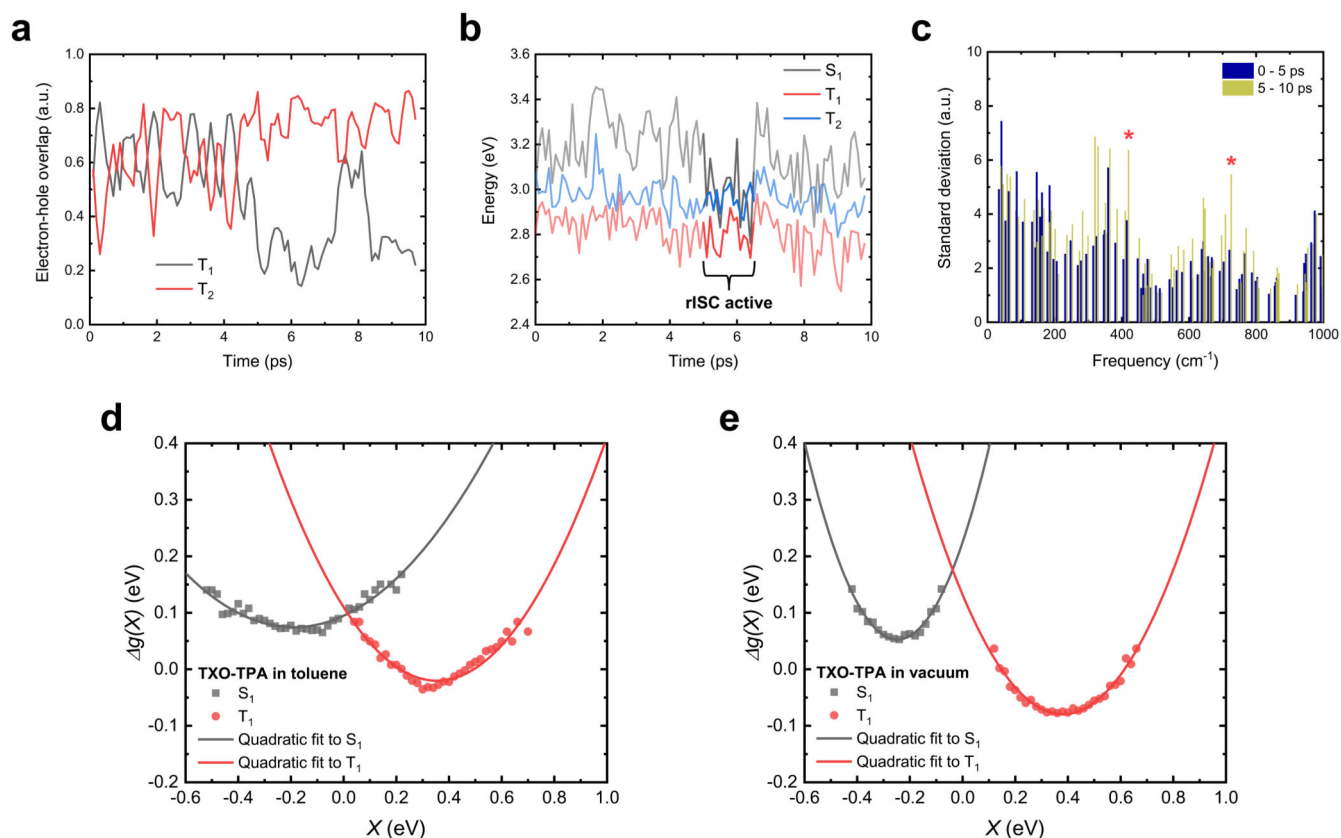


Figure 6. The impact of the toluene solvent dynamics on the reverse intersystem crossing process of TXO-TPA.

(a) The electron/hole overlap for the two lowest energy triplet states, indicating whether they possess primarily ^3LE (large overlap) or ^3CT (small overlap) character during the timescales of the simulation. (b) The energy of the S_1 , T_1 and T_2 states over time timescales of the simulation. The bold section between 5-6.5 ps indicates the region where all three electronic excited states are confined within a narrow energy range, enabling rISC to take place. (c) The standard deviations of the mode intensities computed during the early (0-5 ps) and late (5-10 ps) simulation timescales. Over the later timescales where the solvent has reorganised to stabilise the ^3CT state, clusters of modes around 400 and 700 cm^{-1} become strongly active (as denoted by the red asterisks). (d) Free energy functions for S_1 (back squares) and T_1 (red circles) states together with their quadratic fits for TXO-TPA in an explicit toluene solvent environment. (e) Free energy functions for S_1 (back squares) and T_1 (red circles) states together with their quadratic fits for TXO-TPA in vacuum.